Large eddy simulations for radiation-spray coupling for a lean direct injector combustor

Citation	El-Asrag, H. A., Iannetti, A. C., & Apte, S. V. (2014). Large eddy simulations for radiation-spray coupling for a lean direct injector combustor. Combustion and Flame, 161(2), 510-524. doi:10.1016/j.combustflame.2013.09.020
DOI	10.1016/j.combustflame.2013.09.020
Publisher	Elsevier
Version	Version of Record
Citable Link	http://hdl.handle.net/1957/47491
Terms of Use	http://cdss.library.oregonstate.edu/sa-termsofuse

Combustion and Flame 161 (2014) 510–524

Contents lists available at ScienceDirect

Combustion and Flame

journal homepage: www.elsevier.com/locate/combustflame

Large eddy simulations for radiation-spray coupling for a lean direct injector combustor

Hossam A. El-Asrag [a,*], Anthony C. Iannetti [b], Sourabh V. Apte [c]

[a] Center for Turbulence Research, Stanford University, Stanford, USA
[b] NASA Glenn Research Center, Cleveland, OH, USA
[c] Mechanical Engineering Department, Oregon State University, Corvallis, OR, USA

ARTICLE INFO

Article history:
Received 28 February 2013
Received in revised form 12 May 2013
Accepted 13 September 2013
Available online 15 October 2013

Keywords:
Large eddy simulation
Radiation
Lean direct injection
Turbulent flames
Spray modeling
Stochastic secondary breakup

ABSTRACT

Large Eddy Simulations (LESs) for a lean-direct injection (LDI) combustor are performed and compared with experimental data. The LDI emissions characteristics, and radiation-spray coupling effect on the predictions are analyzed. The flamelet progress variable approach is employed for chemistry tabulation coupled with a stochastic secondary breakup model. Good comparisons are shown with the experimental data mean and root mean square for both the gas phase and spray droplets profiles. The effect of combustion is found to change the shape and structure of the central recirculation zone to be more compact in length but larger in diameter in the transverse direction. In-addition the results show that the gas phase radiation alters the spray dynamics by changing the local gas-phase temperature distribution. This impacts the spray evaporation rate, the local mixture fraction, and consequently the combustion heat released rate and the predicted emissions. The simulation with no radiation modeling shows over prediction in the temperature distribution, pollutants emissions, higher fuel evaporation rate, and narrower range of droplet size distribution with lower number density for the smaller size particles. The current study suggests that, even for low pressure systems, radiation modeling can be important for accurate emissions prediction.

1. Introduction

Modern combustors must balance the need for stability and performance with the goals of higher efficiency and lower emissions. Emissions from gas turbines can have a profound effect on the environment and the balance of the eco-system [1]. For example, green house gases like carbon dioxide CO_2, water vapor H_2O, and methane CH_4 are primary combustion by-products from fossil fuels. These gases contribute to global warming by absorbing the sun's infrared rays and remitting them over time to raise the atmospheric temperature. Other important pollutants are CO, NO_x and particulate matter (PM). While CO has known hazardous health effects, NO causes acidic rain and depletes the ultra-violet protective layer known as the ozone layer [2]. Particulate matter (PM) emissions, both volatile and non-volatile soot (known as black carbon) can reduce visibility, affect cloud formation, and are known for there carcinogenic precursors and associated organics that have direct effect on human heath when inhaled [3].

A common approach to reduce emissions of NO_x, CO, soot, and unburned hydrocarbons is to burn the fuel in lean premixed or partially premixed conditions, which is prone to both dynamic and static flame instabilities [4–6]. For aircraft engines, combustion instability poses a safety concern and must be avoided. Modern engines for next generation transportation aircraft, however, face even more stringent emissions regulations for both NO_x and particulate matter (PM), which poses an engine design requirement of ultra low emission characteristics. To meet this challenge, several engine configurations are proposed that are based essentially on burning the fuel in the premixed or the partially premixed regimes. Among these designs are lean-premixed-pre-vaporized combustion (LPP) and lean direct injection combustion (LDI) [7]. In the current paper we simulate a full single-cup LDI combustor [8,9].

Gas turbine engine's emissions simulations, however, are faced by many challenges [10,11]. In-addition to the wide range of turbulent flow scales introduced at high Reynolds number, gas turbine engines burn complex chemistry fossil fuels for energy production like Jet-A and JP-8. The numerical chemistry models that describe the oxidation of such fuels are highly stiff and usually involves hundreds of species and thousand of reactions that introduce time scales that are much faster than the flow time scales, typically in the order of 10^{-8}–10^{-12} s [12]. The time and space resolution for such enormous amount of scalars will require an ultra fine mesh [13], which leads to a costly prohibitive computation [14–16].

* Corresponding author. Present address: Ansys, Inc., 10 Cavendish Court Lebanon, NH 03766, USA.
E-mail address: hossam.elasrag@ansys.com (H.A. El-Asrag).

0010-2180/$ - see front matter © 2013 The Combustion Institute. Published by Elsevier Inc. All rights reserved.
http://dx.doi.org/10.1016/j.combustflame.2013.09.020

More specifically, pollutants chemistry models expand the number of chemical reactions and species involved and the numerical effort to predict them [17]. The complexity is even exacerbated as most of gas turbine engines fuels are injected in the liquid phase. The liquid fuel jet undergoes primary [18] then secondary breakups before being evaporated by heat transfer from the surrounding gas-phase fluid [19]. The efficiency of the spray atomization controls the local fuel to air ratio and is, therefore, coupled with the rate of pollutants formation and other flow physical process such as radiation [20]. To resolve this multi-scale challenge, efficient numerical tools are needed to simulate such complex physics [21–23] in a computationally affordable manner. Many Large Eddy Simulations (LESs) have been conducted successfully for turbulent reactive flows in gas turbine engines [22] using both structured [24,25,23] and unstructured meshes [19,26]. The current work presents LESs that couple detailed chemistry, spray dynamics, and radiation effects in complex geometry. In-addition, we present one of the most detailed comparisons with the available experimental data for the LDI single cup [27–29]. The LDI configuration is a promising design for modern gas-turbine combustors, where the combined geometry, of a swirler and a Venturi nozzle, results in stable ignition with potentially ultra-low NO_x and soot emissions. The Venturi nozzle provides sufficient residence time for the fuel droplets to vaporize and mix uniformly with the swirled air in a lean mixture [8]. To achieve realistic inflow conditions the full swirl injector is included in the current simulation.

Cost and complexity of simulation have been always two hurdles to account for radiation effect in turbulent reactive flows. However, turbulence-radiation coupling has been investigated for gas-phase reactive flows by many researches using different methodologies. Many Reynolds average Navier Stokes (RANS) simulations exist that address such problem[30–33] and few only using LES [34]. Coelho [35] reviewed numerical simulations for turbulence radiation interaction (TRI). In his research [34], he studied TRI using a stochastic model for the scalar fluctuations and then integrated the radiative heat transfer equation (RTE) along an optical path with a DNS resolution. He showed that turbulent fluctuations contribute to decrease the flame temperature due to radiation below the level observed without fluctuations. Because LES is known to be a better tool to model the subgrid fluctuations, it is expected to provide better estimates for the radiation effect than RANS simulations especially for turbulent flows. Santos et al. [36] proposed a two independent code approach. The LES code communicates the temperature and mass fraction field to a 2D radiation heat transfer code that returns the radiation source term to the LES code using a ray-tracing method to solve the RTE. Similar to the current work conclusion, they found that radiation strongly modify the flame dynamics by reducing the flame temperature and stability, which make the flame more sensitive to turbulence. LES combined with discrete ordinate model (DOM) was also employed by Dejardins and Frankel [37] to simulate 2D non-premixed sooting acetylene-air planar jet flame and for a 3D model gas turbine engine by Jones and Paul [38]. On the other hand the research that studies the spray-radiation coupling in a turbulent environment is very sparse and scattered in the literature [20,39]. To the knowledge of the authors, the current study represents one of the first few full three-dimensional turbulent swirling-flow simulations that address spray-radiation coupling using simplified optically thin radiation model.

The paper is organized as follows. Descriptions of the numerical approach and the associated models (i.e. combustion model, radiation model, and spray model) are outlined in Section 2. Section 3 shows the numerical setup and the initial gas phase and spray conditions. The discussions on the results are shown in Section 4 and finally the conclusions are presented in Section 5.

2. Numerical approach

The simulations are performed by the unstructured Stanford LES code CDP [40]. CDP is a set of massively parallel unstructured finite-volume flow solvers developed specifically for large eddy simulation. A node-based low-Mach number formulation is used to perform the reactive simulations, while a fully incompressible solver is used for the non-reactive flow for computational efficiency. The non-reactive simulation governing equations are shown earlier [41]. The LES reactive governing equations and their sub-grid closures are described in details in [40] and only a brief summary is given here. The gas-phase filtered governing equations are:

$$\frac{\partial \overline{\rho}}{\partial t}+\frac{\partial \overline{\rho}\widetilde{u}_i}{\partial x_j}=\overline{\dot{S}}_m$$

$$\frac{\partial \overline{\rho}\widetilde{u}_i}{\partial t}+\frac{\partial \overline{\rho}\widetilde{u}_j\widetilde{u}_i}{\partial x_j}=-\frac{\partial \overline{P}}{\partial x_i}+\frac{\partial\left(2\overline{\nu}\widetilde{S}_{ij}\right)}{\partial x_j}-\frac{\partial \tau_{ij}}{\partial x_j}+\overline{\dot{S}}_i \tag{1}$$

where the $\overline{()}$ denotes spatial filtering and the $\widetilde{()}$ denotes Favre density-weighted filtering. The gas-phase filtered density, velocity, pressure, strain rate tensor, and dynamic viscosity are $\overline{\rho}, \widetilde{u}_i, \overline{p}$, $\widetilde{S}_{ij}=\frac{1}{2}\left(\frac{\partial \widetilde{u}_i}{\partial x_j}+\frac{\partial \widetilde{u}_j}{\partial x_i}\right)$, and $\overline{\nu}$, respectively. In Eq. (1), $\overline{\dot{S}}_m$ and $\overline{\dot{S}}_i$ are the rates of mass and momentum transport between the gas phase and the spray liquid droplets (described in Section 2.4). The filtered temperature, density, and species mass fractions are computed by the equation of state formulated by the flamelet progress variable model [42] (described in Section 2.1). In Eq. (1) the dynamic Smagorinsky model is used for closure of the residual shear stresses τ_{ij} [43].

For accurate chemistry modeling, a detailed Jet-A surrogate mechanism is utilized [44] and tabulated a priori for the LES simulations in the steady flamelet frame-work [42]. The number of species and reactions considered are 118 and 900, respectively. Because radiation and NO_x productions are known to have slower time scales compared to the fast chemistry assumption utilized in the flamelet assumption [45], a transport equation for NO_x mass fraction and for sensible heat loss parameter are solved with the flow field rather than extracting their values from the flamelet tables [46]. The gas-phase combustion model is coupled with spray atomization by a stochastic subgrid model for spray secondary breakup [47,19]. The next sections describe briefly the modeling approach.

2.1. Combustion modeling

The combustion model employed here is the flamelet/progress-variable (FPV) [42,48,49,45]. The FPV approach is based on the flamelet concept [21], where the turbulent non-premixed flame is viewed as an ensemble of laminar flamelets. The laminar flamelet concept assumes fast chemistry or high Damköhler number, which is a suitable assumption for gas turbine engines flows with swirl injection [21]. The solution of each flamelet on a canonical one-dimensional presentation can be parameterized on a lower dimension manifold, which relates the thermochemical state vector (i.e. species mass fractions, density, and temperature) to few parameters (i.e. the mixture fraction and a chemical progress parameter). The laminar flamelet equations are derived in the mixture fraction space [21] for a unity Lewis number assumption:

$$\rho\frac{\partial \Phi}{\partial t}-\rho\frac{\chi}{2}\frac{\partial^2 \Phi}{\partial Z^2}=\dot{\omega}, \tag{2}$$

where Z is the mixture fraction, ρ is the density, $\Phi=(T, y_i)^T$ is thermochemical state vector for the species mass fractions y_i and the temperature $T, \dot{\omega}$ is the corresponding source-terms vector,

$\chi = 2D|\nabla Z|^2$ is the scalar dissipation rate, and D is the diffusivity. The scalar dissipation rate is directly impacted by the flow large scale turbulent structures and, therefore, is an inertial range invariant that has to be modeled. It represents the effect of the resolved turbulent vortices strain rate imposed on the **Z** field: for example if a turbulent vortex imposes a compressive strain, the scalar dissipation rate will increase, and more heat and mass diffuses from the flame inner layer and the flame temperature decreases, which ultimately leads to flame extinction. From that perspective, Eq. (2) characterizes the non-linear interactions between chemistry and the scalars transport in the mixture fraction space. The mixture fraction, by definition, is a conserved quantity [50], however, it is not strictly conserved in spray combustion [20,51] and further assessment for the flamelet concept is needed to account for the rate of fuel evaporation [39].

In the steady laminar flamelet model (SLFM) the solution of Eq. (2) (without the unsteady term) is tabulated as a function of the mixture fraction, that varies from 0 in the oxidizer stream to 1 in the fuel stream, and a set of predefined scalar dissipation rates. The flame surface is then identified as the location of the stoichiometric mixture fraction $Z(x,t) = Z_{st}$ and the thermochemical scalars solution vector Φ is parameterized as function of Z and χ:

$$\Phi = \mathcal{F}_{\Phi}(Z, \chi). \tag{3}$$

where $\mathcal{F}_{\Phi}$ is a functional relation that describes Φ as a function of the SLFM variables (Z and χ). In reality this is a single variable formulation in the mixture fraction, and leads to a single burning solution for each flamelet. Therefore, in SLFM only non-extinguished solutions of the flamelet equations are considered, which limits the applicability of the model. It was shown by Pierce and Moin [42], for example, that SLFM predicts too much heat release in the essentially non-reactive regions close to the nozzle for a flame that is aerodynamically stabilized by a recirculation region.

To overcome this limitation, Pierce and Moin [42] proposed a tabulation based on the mixture fraction and a reaction progress parameter λ instead of the scalar dissipation rate, which leads to the Flamelet/Progress Variable (FPV) formulation. The purpose of this parameter is to parameterize the other flame solution stats for Eq. (2) (i.e. fully burning state, transient solution between burned and unburned states, and the unburned state). Because these parameter can be defined in many ways, [42] related λ to a reaction progress variable $\mathcal{C}$, that can be defined as a linear sum of a set of product species mass fractions. Consequently, the new state vector is given as [46]:

$$\Phi = \ominus_{\Phi}(Z, \lambda), \tag{4}$$

where $\ominus$ is the new FPV relationship that contains the other possible burned and unburned solution. The progress variable $\mathcal{C}$ in the current work is defined as linear sum of the mass fractions of CO_2, CO, H_2O, and H_2. By definition, the progress variable $\mathcal{C}$ is a subset of Φ and can be written as:

$$\mathcal{C} = \ominus_{\Phi}(Z, \lambda), \tag{5}$$

Eq. (5) is nonlinear and relates $\mathcal{C}$ and λ with no information on how this functional relation is described. Therefore, the reaction progress parameter λ is defined for each flamelet as the stoichiometric value of the reaction progress variable $\mathcal{C}$ [46] and λ can be obtained from an inversion of Eq. (5):

$$\lambda = \ominus_{\Phi}^{-1}(Z_{st}, \mathcal{C}_{st}), \tag{6}$$

where the subscript st stands for stoichiometric conditions. Eq. (6) assumes that the inversion is unique for the FPV relation ($\ominus$). More discussion on the limitations and assumptions of the FPV is beyond the scope of the current paper.

From Eq. (6) the mean reaction progress parameter $\widetilde{\lambda}$ is replaced by $\widetilde{C}$ and filtered transport equations for the filtered mixture fraction $\widetilde{Z}$ and the filtered progress variable are solved simultaneously with Eq. (1):

$$\frac{\partial \bar{\rho}\widetilde{Z}}{\partial t} + \nabla \cdot \left(\bar{\rho}\widetilde{u}\widetilde{Z}\right) = \nabla \cdot \left(\bar{\rho}\widetilde{D}\nabla\widetilde{Z}\right) + \nabla \cdot \widetilde{\tau}_z^{res}, \tag{7}$$

$$\frac{\partial \bar{\rho}\widetilde{C}}{\partial t} + \nabla \cdot \left(\bar{\rho}\widetilde{u}\widetilde{C}\right) = \nabla \cdot \left(\bar{\rho}\widetilde{D}\nabla\widetilde{C}\right) + \nabla \cdot \widetilde{\tau}_c^{res} + \bar{\rho}\widetilde{\dot{\omega}}_C. \tag{8}$$

where $\widetilde{D}$ is the filtered molecular diffusivity, assuming equal species diffusivity and unity Lewis number, and $\widetilde{\dot{\omega}}_C$ is the filtered chemical source term of the progress variable tabulated in the flamelet library. The unclosed residual stresses $\widetilde{\tau}^{res}$ are modeled by a dynamic approach [42]. The mixture fraction variance is computed using an algebraic model [42,22], which assumes homogeneity and local equilibrium for the subgrid scales:

$$\bar{\rho}\widetilde{Z''^2} = C_Z \Delta^2 \bar{\rho} \mid \nabla\widetilde{Z}|^2, \tag{9}$$

where the mixture fraction coefficient C_Z is computed dynamically [42,22] and $\overline{\rho}$ is the filtered density.

2.2. Radiation and NO modeling

For accurate temperature and pollutant predictions, radiation heat transfer has to be considered. [46] have extended the FPV approach described in Section 2.1 to account for radiation and NO_x formation. The radiation and NO_x formation time scales are slow [52] compared to other thermochemical state variables production rates that assume fast chemistry, and cannot be accounted for using the steady flamelet approach. Therefore, in this extended FPV approach transport equations for the filtered sensible enthalpy ($\widetilde{H}$) and NO_x mass fraction ($\widetilde{Y_{NO}}$) are solved with the flow field, presumably, to account for the flow unsteadiness effect on these two parameters. The final form of the extended FPV equation of state (EOS) can then be written as follows:

$$\widetilde{\Phi} = \ominus_{\widetilde{\Phi}}\left(\widetilde{Z}, \widetilde{Z''^2}, \widetilde{C}, \widetilde{H}\right). \tag{10}$$

Consequently, in-addition to the transport equations for $\widetilde{Z}$, and $\widetilde{C}$, a transport equation is solved for the filtered enthalpy $\widetilde{H}$:

$$\frac{\partial \bar{\rho}\widetilde{H}}{\partial t} + \nabla \cdot \left(\bar{\rho}u\widetilde{H}\right) = \nabla \cdot \left(\bar{\rho}\widetilde{D}\nabla\widetilde{H}\right) - \widetilde{\dot{q}}_r, \tag{11}$$

A simplified optically thin radiation model [53] is considered here for the filtered radiation source term:

$$\widetilde{\dot{q}}_r = 4\sigma\left(\widetilde{T^4} - \widetilde{T}_{\infty}^4\right)\sum(\widetilde{\mathbf{p_i}\mathbf{a_i}}), \tag{12}$$

where $\mathbf{p}_i$ and $\mathbf{a}_i$ are the partial pressure and Planck mean absorption coefficient of species i, respectively, σ is the Stefan Boltzmann constant, and T_{∞}^4 is the ambient reference temperature at one atmosphere. The absorption coefficients in Eq. (12) account for the radiation emitted from CO_2, H_2O, CO, and CH_4 species. It is worth mentioning that although the optically thin radiation model is computationally affordable, it is a simplified model that assumes an unimpeded isotropic view of the flame to the cold surroundings and therefore absorption and scattering by the surrounding media are neglected. The radiation model assumptions might have an impact on the results accuracy. For large eddy simulations, however, under lean conditions, where usually the wall heat transfer effect is not resolved, and no soot particulates are emitted, the assumption of optically thin flame is reasonable as the surrounding media provides less amount of scattering and absorption [54]. Watanabe et al. [20], for example, used DO method to model radiation in a

2D laminar sooting counter flow diffusion flame and observed that without the radiation modeling, flame temperature and soot volume fraction are greatly overestimated (about 300–400 K). More sophisticated radiation models like the Discrete Ordinate (DO) model or the Monte Carlo Ray-Trace method (MCRT) will add tremendous computational effort to the simulation.

To account for the NO_x production, the filtered mass fraction of NO ($\widetilde{Y}_{NO}$) is computed by solving a transport equation rather than extracting the values from the flamelet tables directly [46]:

$$\frac{\partial \bar{\rho}\widetilde{Y}_{NO}}{\partial t} + \nabla\cdot\left(\bar{\rho}u\widetilde{Y}_{NO}\right) = \nabla\cdot\left(\bar{\rho}\widetilde{D}\nabla\widetilde{Y}_{NO}\right) + \bar{\rho}\dot{\widetilde{\omega}}_{NO}. \tag{13}$$

Here the filtered net production rate $\dot{\widetilde{\omega}}_{NO}$ is closed by assuming that scale similarity between the NO mass fraction computed from Eq. (13) and the steady tabulated values. In-addition, if all the species that contribute to the formation of NO occur on short time scales and can be extracted from the FPV table then the source term is written in the following form [46]:

$$\dot{\widetilde{\omega}}_{NO} = \dot{\widetilde{\omega}}^{+}_{NO} + \widetilde{Y}_{NO}\frac{\dot{\widetilde{\omega}}^{-}_{NO}}{\widetilde{Y}^{FPV}_{NO}}. \tag{14}$$

Here, the superscripts FPV "+" and "−" refers to values extracted from the FPV table, production source terms and destruction source terms, respectively. Finally, the filtered Eqs. (7), (8), (11), and (13) are solved simultaneously with Eq. (1) at each LES integration time step. The filtered quantities, Z, H, and C together with the Z variance ($\widetilde{Z''^2}$) are used to access the EOS given by Eq. (10). The turbulence closure for the extracted thermodynamic variables from the EOS is shown next.

2.3. Combustion subgrid closure

From Eq. (10) all the filtered thermochemical variables $\widetilde{\Phi}$ are function of the four parameters ($\widetilde{Z}, \widetilde{\mathcal{H}}, \widetilde{\mathcal{C}}$, and $\widetilde{Z''^2}$) computed from three transport equations (Eqs. (7), (8), and (11)) and an algebraic relation (Eq. (9)). To account for the subgrid fluctuations, a presumed PDF approach is employed [22]. Following the discussion in Section 2.1 for the progress variable $\mathcal{C}$, a similar parameter to λ can be assumed for the enthalpy $\mathcal{H}$ (named Υ hereafter). Assuming that Υ, λ, and Z are independent, the joint probability density function (PDF) between $\mathcal{C}, \mathcal{H}$, and Z is evaluated to obtain the Favre filtered ($\widetilde{}$) values of the state vector Φ:

$$\widetilde{P}(Z,\lambda,\Upsilon;\mathbf{x},\mathbf{t}) = \widetilde{\mathbf{P}}(\lambda \mid \mathbf{Z};\mathbf{x},\mathbf{t})\widetilde{\mathbf{P}}(\Upsilon \mid \mathbf{Z};\mathbf{x},\mathbf{t})\widetilde{\mathbf{P}}(\mathbf{Z};\mathbf{x},\mathbf{t}), \tag{15}$$

where the marginal PDF of the mixture fraction $\widetilde{P}(Z)$ is assumed to be a beta distribution [42], and the conditional progress parameters PDFs ($\widetilde{P}(\lambda \mid Z;\mathbf{x},t)$ and $\widetilde{P}(\Upsilon \mid Z;\mathbf{x},t)$) are assumed to be delta functions. The delta function assumption, restricts the length scale of each flamelet to be in the order of the LES grid size or larger [42]:

$$\widetilde{P}(Z,\lambda,\Upsilon;\mathbf{x},\mathbf{t}) = \beta\left(\mathbf{Z};\widetilde{\mathbf{Z}},\widetilde{\mathbf{Z''^2}}\right)\delta(\lambda-\widetilde{\lambda\mid\mathbf{Z}})\delta(\Upsilon-\widetilde{\Upsilon\mid\mathbf{Z}}). \tag{16}$$

The β-distribution is characterized by the mixture fraction mean $\widetilde{Z}$ and the mixture fraction variance $\widetilde{Z''^2}$, while the delta-function-PDF is characterized by the mean of the reaction progress variable $\widetilde{\mathcal{C}}$ and enthalpy $\widetilde{\mathcal{H}}$. Consequently, the flamelet tabulation is also function of these parameters.

2.4. Secondary breakup spray model

In the LDI configuration, Jet-A fuel spray droplets are injected from a centerline simplex atomizer, with a specified drop-size distribution and a hollow cone spray with a total angle of 90°. Therefore, during the simulation, the spray atomization and evaporation processes have to be modeled in the LES framework. The spray models employed have been described in detail by Apte et al. [47,19,55]. Here, we summarize the most important features for completeness. In the following, the droplet transport and evaporation rate models are described in Section 2.4.1, then the stochastic breakup model in Section 2.4.2.

2.4.1. Droplet transport and evaporation models

Droplet dynamics are simulated using a Lagrangian point-particle model. Three basic assumptions are inherent in the model: i.e. the density of the Jet-A droplets are much larger than that of the fluid surrounding it ($\rho_p/\rho_g \sim 10^3$), the droplet-size is always small compared to the turbulence integral length scale, and that the effect of shear on the droplet motion is negligible. The high value of density ratio implies that the Basset force and the added virtual mass terms [56] are small and are therefore neglected. Under these assumptions, the Lagrangian equations governing the droplets motions become:

$$\frac{d\mathbf{x}_p}{dt} = \mathbf{u}_p; \frac{d\mathbf{u}_p}{dt} = D_p(\mathbf{u}-\mathbf{u}_p) + \left(1-\frac{\rho_g}{\rho_p}\right)\mathbf{g}, \tag{17}$$

where x_p is the droplet position in space, $\mathbf{u}_p$ the droplet velocity components, $\mathbf{u}$ gas-phase velocities interpolated to the droplet location, ρ_p and ρ_g the droplet and gas-phase densities, $\mathbf{g}$ is the gravitational acceleration, and D_p is the inverse of the droplet relaxation time-scale (τ_p).

The droplet evaporation model is based on an equilibrium 'uniform-state' model for an isolated droplet [57–59]. Miller et al. [60] investigated different models for evaporation accounting for non-equilibrium effects. Advanced models considering internal circulation, temperature variations inside the droplet, effects of neighboring droplets [59] may alter the heating rate (Nusselt number) and the vaporization rates (Sherwood number). However, for the present case evaporation is dominated by mass-diffusion, which has low rates, and hence these effects are neglected. For the uniform-state model, the Lagrangian equations governing droplet temperature and mass can be formulated as [57–59]:

$$\frac{dm_p}{dt} = -\frac{m_p}{\tau_m}; \frac{dT_p}{dt} = \frac{1}{\tau_c}\left(T_{g,p}-T^s_p\right) - \frac{1}{\tau_m}\frac{\Delta h_v}{C_{p,\ell}} \tag{18}$$

where Δh_v is the latent heat of vaporization, m_p mass of the droplet, T_p temperature of the droplet, T^s_p is the temperature at the droplet surface, $T_{g,p}$ is the temperature of the gas-phase at the droplet location and $C_{p,\ell}$ is the liquid specific heat. The diameter of the droplet is calculated from its mass, $d_p = (6m_p/\pi\rho_p)^{1/3}$. Here, τ_m and τ_c are the droplet life-time and the convective heating time-scales respectively, and are given as:

$$\frac{1}{\tau_m} = \frac{12}{d^2_p}\mathcal{D}^s\ln(1+B_Y)\mathrm{Sh}; \frac{1}{\tau_c} = \frac{12}{\rho_p d^2_p}\frac{k^s}{C_{p,\ell}}\frac{\ln(1+B_T)}{B_T}\mathrm{Nu}. \tag{19}$$

Here, $\mathcal{D}$ and k are the diffusivity and conductivity, respectively. The superscript s stands for droplet surface and Sh and Nu are the Sherwood and Nusselt numbers defined as:

$$\mathrm{Sh} = 1 + \frac{0.278Re_p^{1/2}[Sc^s]^{1/3}}{\sqrt{1+1.232/Re_p}[Sc^s]^{1/3}}; \quad \mathrm{Nu} = 1 + \frac{0.278Re_p^{1/2}[Pr^s]^{1/3}}{\sqrt{1+1.232/Re_p}[Pr^s]^{1/3}}. \tag{20}$$

where B_Y and B_T are the mass diffusion and heat transfer coefficients, respectively. For $T^s_p < T_b$ (where T_b is the boiling point), $B_Y = (Y^s_F - Y_{Fg,p})/(1-Y^s_F)$ and $B_T = C^s_p(T_{g,p}-T^s_p)/(\Delta h_v)$, where $Y_{Fg,p}$

is the fuel vapor mass-fraction interpolated to the droplet location. For $T_p^s \geqslant T_b, B_Y$ is set equal to B_T, and the fuel mass-fraction Y_F is computed from the Clausius–Clapeyron equilibrium vapor–pressure relationship. In each cell node the multi-phase source terms in Eq. (1) are computed as the ensemble average of all the tracked particles mass and temperature variations. A third-order Runge–Kutta scheme is used to integrate the above set of ODEs with the minimum physical drop time scale [19].

2.4.2. Stochastic droplet breakup

A stochastic subgrid model for spray atomization is used here. The initial liquid film is approximated by a droplet of size equal to the nozzle diameter. The model views the subsequent particle breakup of the injection of a specified drop-size as a discrete random process, where droplet size is treated as a time-dependent stochastic variable. The temporal and spatial evolution of the particle size distribution is then governed by the Fokker–Plank differential equation. This evolution leads to the formation of new droplets and destruction of the parent ones. The new droplets position and velocity vectors are tracked by a Lagrangian algorithm in the physical space as described in Section 2.4.1. Two-way coupling between the gas phase and the liquid droplets is achieved by the source terms in the gas-phase equations, which represent the mutual effect of mixing and momentum/energy transport. These effects are induced by droplet breakup, evaporation, and convection by the flow-field.

Simultaneously with the process of secondary droplet breakup and mixing with the gas phase, the liquid phase evaporates under the appropriate conditions. The evaporation model solves a set of ordinary differential equations (ODEs) that describe the variation of the droplet mass and temperature due to evaporation and assumes that non-equilibrium effects inside the droplet volume are neglected as described in Section 2.4. A third-order Runge–Kutta scheme is used to integrate the set of ODEs with the minimum physical drop time scale. The mathematical formulation of the above scheme is omitted here for brevity and can be found elsewhere [55].

3. Numerical setup

The experimental setup and data are provided by Farhad et al. [61]. The geometry of the single-element combustor is shown in Fig. 1a with the inflow pipe upstream of the swirler. Liquid fuel is injected through the center (closed for the non-reactive case), while air is injected through a swirler with vane angles of 60°. The global swirl number is unity. The swirler is composed of six helical vanes with an inside diameter of 9.3 mm and an outside diameter of 22.1 mm and an effective area of 870 mm^2. The fuel droplets from the centerline and the swirled air are mixed in a converging–diverging Venturi nozzle. The combustor has a square cross-sectional area of 50.8 × 50.8 mm.

The mesh uses 1,072,640 hexahedral elements, which is slightly above the 861,823 element mesh used in the RANS calculations [61,62] and about half the LES structured mesh used by Patel and Menon [25]. Only local grid refinement between the Venturi exit cross section and the location $X = 3$ mm is attempted with no significant changes observed in the flow field. The current grid resolution might have an effect on the results and a full grid dependency study, although computationally prohibitive, will be optimum. However, compared to all the published data in the literature, for the same test case, the current paper comparisons with experimental profiles show good matching and therefore, further mesh refinement is not critical for our study. The unstructured mesh is shown in Fig. 1. The mesh distribution along the $z = 0$ plane and in the vanes is shown in Fig. 1b, while the y–z plane grid

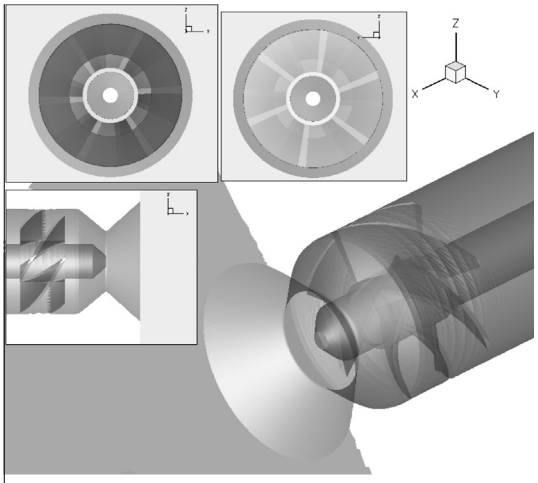

(a) LDI geometry

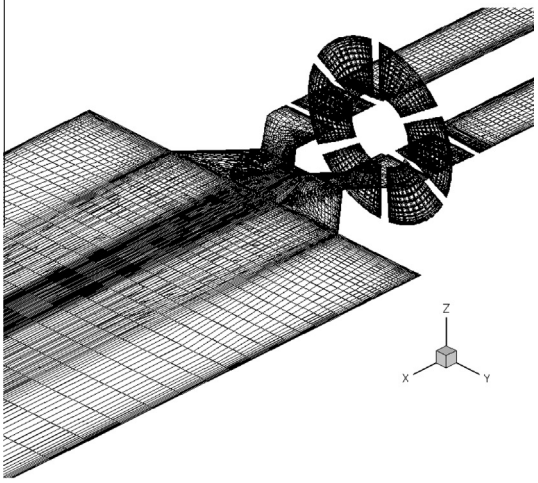

(b) The vanes and the y-x mesh plane

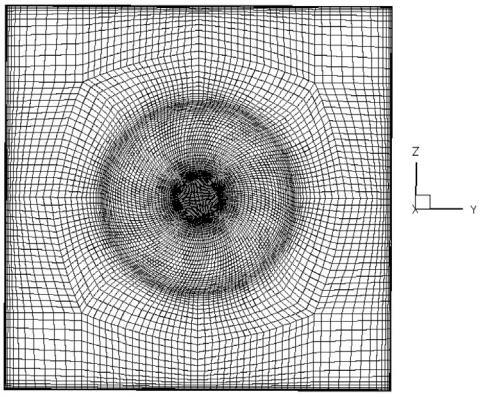

(c) y-z mesh plane

Fig. 1. The LDI single element geometry and unstructured hexahedral mesh.

distribution is presented in Fig. 1c. The mesh cells are clustered toward the centerline and toward the walls of the combustor.

An inflow bulk velocity of 20.14 m/s is provided through a tube upstream of the swirl injector. The inflow air is at temperature $T_o = 294$ K and pressure of 1 atm, while the global equivalence ratio is 0.75. The fuel spray has an inflow mass flow rate of 4.15×10^{-04} kg/s and an initial velocity of 20 m/s. The droplets are injected with a Rosin–Rammler distribution

$$F_m(D) = 1 - \exp\left(-\left(\frac{D}{\delta}\right)^n\right), \quad (21)$$

where $F_m(D)$ is the cumulative distribution function of the droplet diameter D, and the parameters $n = 1.34$ and $\delta = 24$ μm are chosen to curve-fit the distribution of the experimental data at the first measured location ($x = 3$ mm). An inflow recycling technique is used [41] to achieve realistic inflow turbulence. The recycling is done until the inflow profile of the upstream pipe recovers a realistic inflow turbulent boundary layer. The boundary conditions used are inflow/outflow in the x-direction and adiabatic walls in the y and z directions.

Statistics are collected over a physical time of 0.032 s after the initial transient for the reactive flow cases and over 0.167 s for the cold-flow case. Based on the bulk inflow velocity and the full length of the combustor, this represents two complete flow-through times for the reactive cases and about seven flow-through times for the non-reactive case. The simulation was performed on a Linux cluster at Stanford University with infiniband interconnection and dual Intel Clovertown (Quad Core) 2.33 GHz processors with 8 GB RAM per node. With the current mesh resolution the code scaling was found to level off at 96 processors for the spray-combustion case. The computational time per flow through time was 900 CPU hours for the reactive case.

4. Results and discussion

In this section, two reactive flow large eddy simulations are compared to the experimental data. Selected non-reactive flow data are shown to highlight the effect of heat release on the flow field. The statistics for the two reactive flow simulations, with and without radiation, are collected over the same total simulation run time. Unless mentioned otherwise, the experimental profiles are compared to the LES profiles with radiation modeling. Almost all available experimental LDI measurements are compared in the current work. The current presentation represents one of the most complete comparisons for the LDI with experiments. First, instantaneous and time averaged results will be shown for the flow field structure and the spray characteristics. Following that the time-averaged flow features of the reactive flow will be compared with the non-reactive case with an emphasis on the radiation modeling effect on the predictions. Finally, the mean and root mean squared (rms) radial and centerline profiles of the gas flow-field, the scalars, and the spray droplets will be compared with the experimental measurements.

4.1. The LDI flow field structure

Figure 2a and b shows iso-surfaces of zero mean axial velocity ($\langle\overline{U}\rangle = 0$ m/s) for both the reactive and non-reactive cases, respectively, where the brackets denote a time average. Due to the flow swirling, an adverse pressure gradient is generated in the axial direction and a vortex breakdown bubble (VBB) is established. The LDI is characterized by a central recirculation zone (CRZ) in addition to recirculation zones (RZs) at the corner of the dump plane. A smaller circulation zone is also observed at the Venturi exit in the non-reactive case. The same three RZs had been reported previously in the non-reactive simulations [41,62]. The length of the CRZ in the non-reactive case is approximately twice as that in the reactive one. However, the reactive CRZ has a larger effective bulk diameter. A small toroidal RZ close to the divergent part of the Venturi is also observed in the reactive flow case as shown by the side views in Fig. 3 and the cross sectional plane in Fig. 4. The more compact and wider reactive CRZ is due to the flow-field expansion by the combustion heat release, which alters the adverse pressure gradient downstream of the injector. This

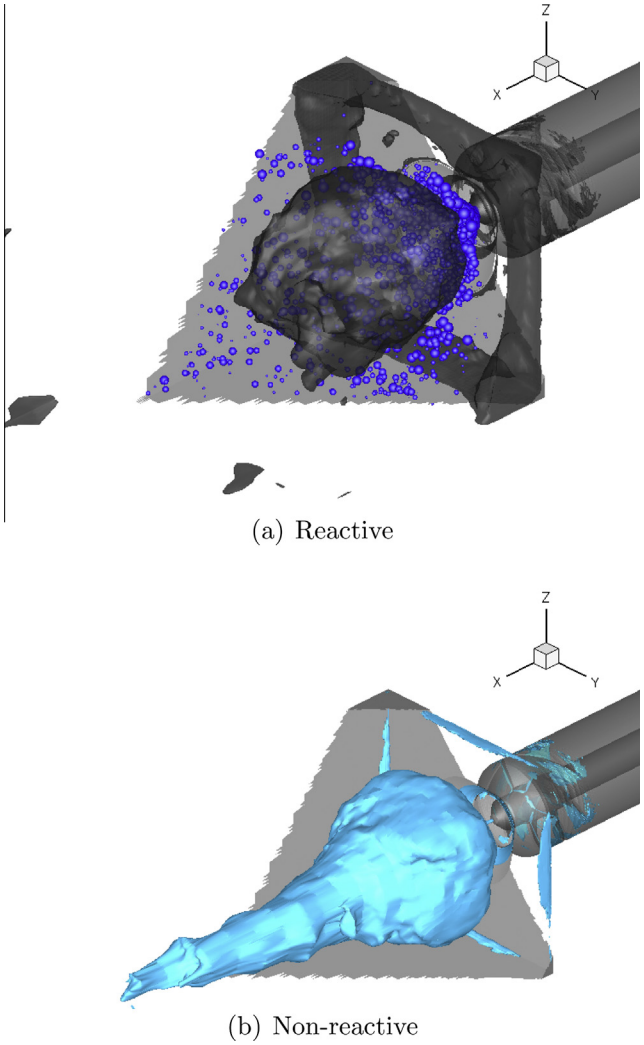

Fig. 2. Iso-surface of the zero time-averaged axial velocity ($\langle\overline{U}\rangle = 0$ m/s). Different color coding is used for the two cases. (For interpretation of the references to color in this figure legend, the reader is referred to the web version of this article.)

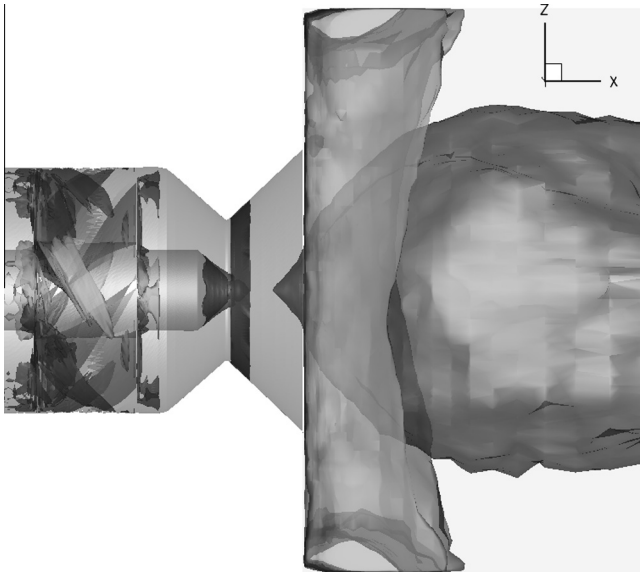

Fig. 3. Side view ($y = 0$ plane) to the central recirculation zone (CRZ) for the reactive flow case viewed by iso-surface of the zero time-averaged axial velocity.

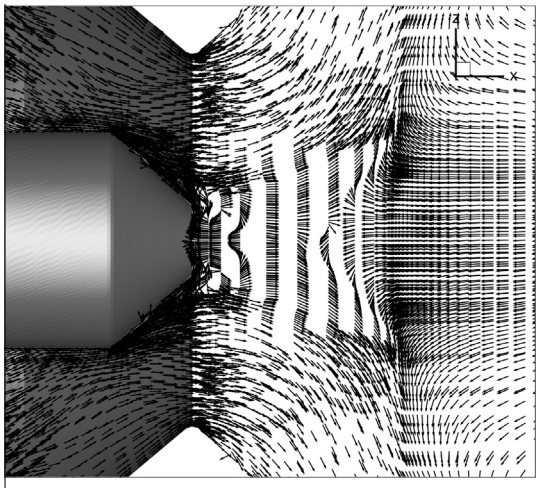

(a) Zoom of the injector area.

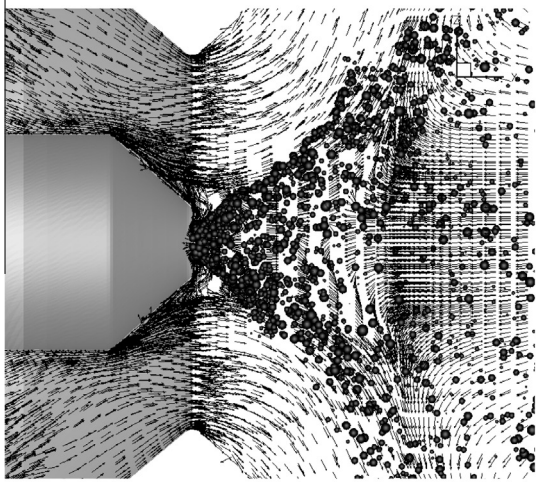

(b) Zoom of droplet distribution scaled by the droplet diameter in the injector area.

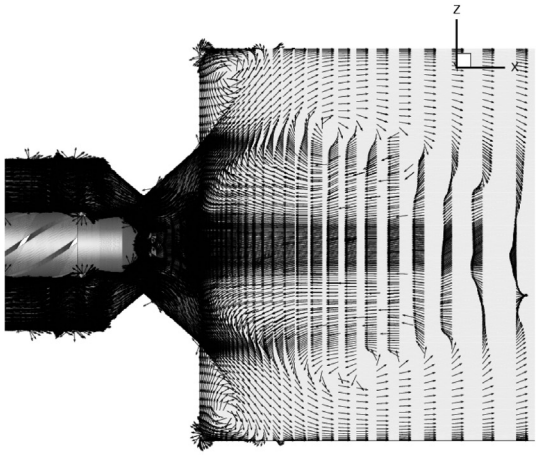

(c) The vortices around the CRZ and at the corners.

Fig. 4. Three vector plots for the mean velocity magnitude projected on the cross-sectional plane $y = 0$ for the reactive flow case with radiation.

conclusion will also be emphasized when comparing the time averaged data.

The above discussion can be clarified more by investigating the velocity vector plots. Figure 4 shows vector plots for the time-averaged total velocity magnitude for the reactive flow case with radiation modeling. Only the vectors projections on the cross-sectional plane $y = 0$ are shown for clarity. Figure 4a and b show a zoom in the venturi and atomizer area with and without spray droplets, respectively, while Fig. 4c zooms out to show the area downstream the Venturi. From Fig. 4a it can be observed that the CRZ starts early inside the divergent part of the Venturi nozzle, in addition to a small RZ observed just downstream of the spray injector exit cross section. These two small RZs inside the Venturi are expected to enhance the spray atomization and the droplets mixing with the swirling air. Figure 4b shows that at the injector exit, the droplets and the spray sheet have enough momentum to penetrate the small RZ toward the Venturi. This observation will be confirmed later by the axial and radial velocity profiles. Figure 4c shows the velocity magnitude vector plot downstream of the venturi outflow cross-section. It is observed that the CRZ has an azimuthal vortex at the location $x = 17$ mm and an additional annular vortex at the burner corners where the second RZ is located. The corner vortices are found to extend along the combustor wall corners up to the combustor exit cross-section in the y–z plane (not shown here), which will alters the spray distribution as shown later. The CRZ structure is an important mechanism to achieve stable combustion and self-ignition during flight for aircraft engines. The dynamics of this stability mechanism is discussed in the next paragraph.

To investigate the flame interaction with the CRZ, the instantaneous temperature distributions are shown in Fig. 5a–d at the cross-sectional plane $y = 0$ in Fig. 5a and at three consecutive instantaneous snapshots at the plane $x = 11$ mm in Fig. 5b–d, respectively. Figure 5a and b are compared at the same time instant. The figures show the dynamic interaction between the flame and the recirculation zone. The highest temperature gradients (i.e. the flame boundaries) are found to be at the interface between the shear layer and the cold inflow at the circumferential irregular profile of the CRZ. At this locations strong mixing is expected between the fresh reactants and the products inside the CRZ, which acts as a natural static stability mechanism for the combustor to avoid flame extinction. At the edge of the CRZ, fresh cold gases (dark areas in Fig. 5b–d) are entrained from the reactants into the CRZ where it ignites inside the core of the RZ. Due to the strong mixing at the CRZ's center, the temperature shows nearly uniform distribution at the center region. This unsteady mechanism, where reactants are entrained inside the CRZ to undergo combustion, ensures flame stability with time, an important requirement for aircraft engines.

4.2. The effect of radiation modeling on the spray characteristics

The effect of radiation modeling on the spray and the scalar field characteristics are investigated. The subsequent effect on the mean scalar field predictions follows this discussion. It is worth mentioning that all our conclusions are in the context of the underlying models assumptions. The following results are naturally contaminated by the errors produced from the subgrid models and the error propagation in the time averaged statistics. Two snapshots of the droplets distribution sized by the droplets mass are shown in Fig. 6 combined with the temperature spectrum. The spray exhibits a 90° cone angle. Some of the spray droplets are trapped inside the corner vortex, which results in an increase in the mean droplet diameter close to the walls. The simulation with radiation shows a wider range of droplet sizes and a lower peak instantaneous temperature. For the shown instantaneous snapshots with radiation, droplet size ranges between 0.5 μm and 50 μm, while without radiation the range is between 0.7 μm and 40 μm. Radiation acts

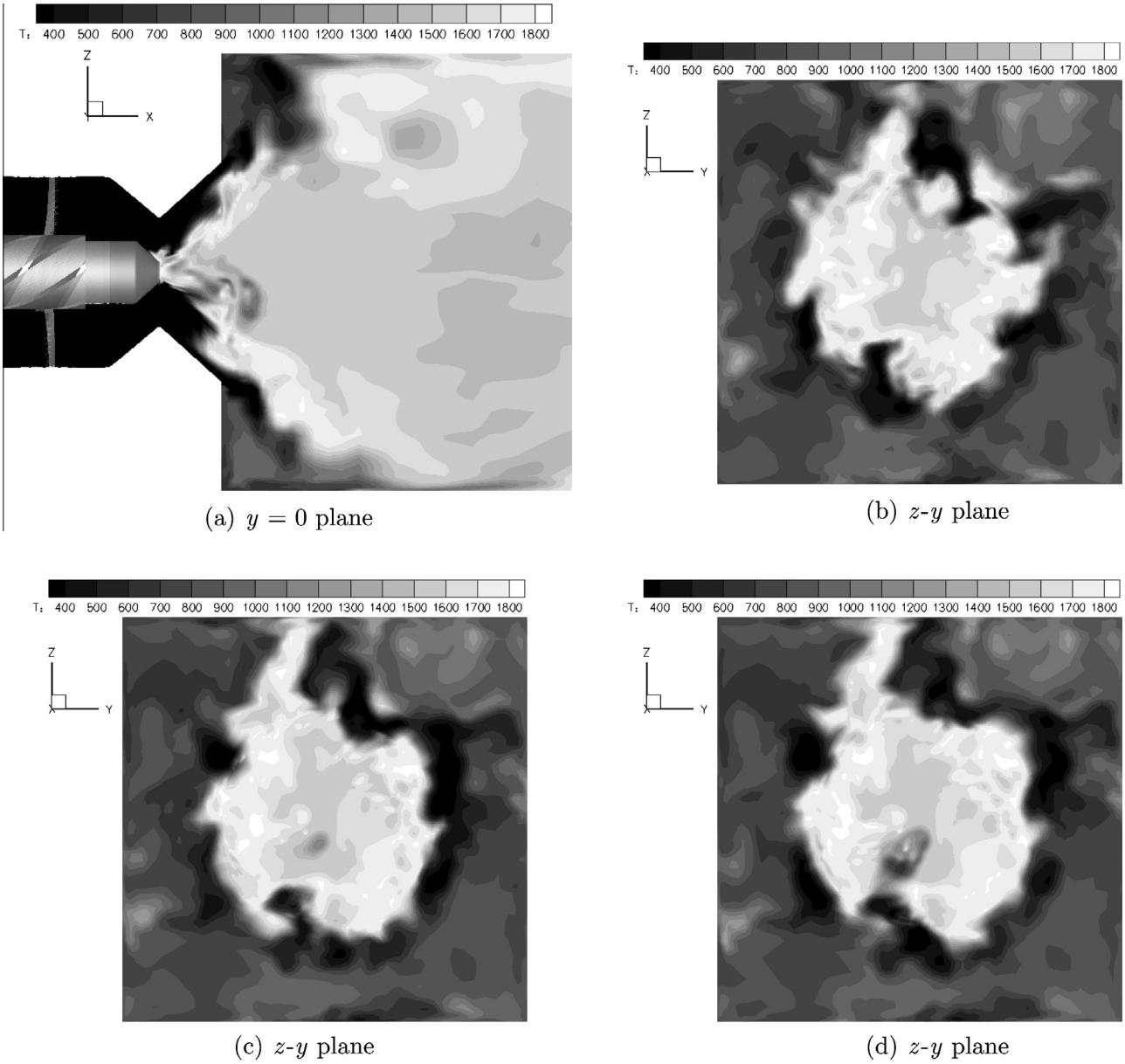

Fig. 5. Instantaneous temperature distribution for the case with radiation. (a) For the z–x plane, (b), (c) and (d) for the z–y plane at three consecutive time snapshots at $x = 11$ mm.

as en energy sink and lowers the local temperature distribution, which results in over-predicted evaporation rate when radiation is not included. This aspect will be discussed in more details using the averaged statistics. Because no primary breakup model is employed here, the spray spectrum shows an intermediate regime, where the spray injected from the nozzle undergoes secondary breakup, followed by a dilute regime downstream of the dump plane where the droplets undergo evaporation. Primary atomization is difficult to model owing to the increased grid resolution needed to capture the interface instabilities [63,18]. The intermediate regime is mainly inside the Venturi, while the dilute regime extends until all the droplets are evaporated about 1–2 combustor diameters downstream the Venturi.

Figure 6, discussed above, indicates that radiation modeling affects locally both the scalar temperature field and the spray characteristics. The radiation effect on mean droplet evaporation rate in kg/s is shown in Fig. 7, where the time-averaged rate of droplet mass evaporation rate at the cross-sectional plane $y = 0$ is compared with radiation modeling in Fig. 7a and without radiation in Fig. 7b. The droplet mass evaporation rate represents the time average of the source term of the droplets mass time variation equation discussed in Section 2.4.1. Without radiation modeling, higher evaporation rates are observed especially in the vicinity of the injector and at the flame surface boundaries. The over-prediction in the evaporation rate can be attributed to higher local temperature, as shown in Fig. 6, or larger available droplet surface area per unit mass. The latter is equivalent to fewer large size droplets or higher number density of smaller size droplets with larger surface area. In our study, only gas phase radiation is accounted for. The dispersed phase radiation effect was studied by Watanabe et al. [20]. In this study 2D simulations for a sooting counter flow flame are performed for three cases using the DO method: with both gas phase and dispersed phase radiation modeling, with no radiation modeling, and with gas phase radiation modeling only. The study shows that gas-phase radiation modeling has the main contribution on the dispersed phase evaporation rate.

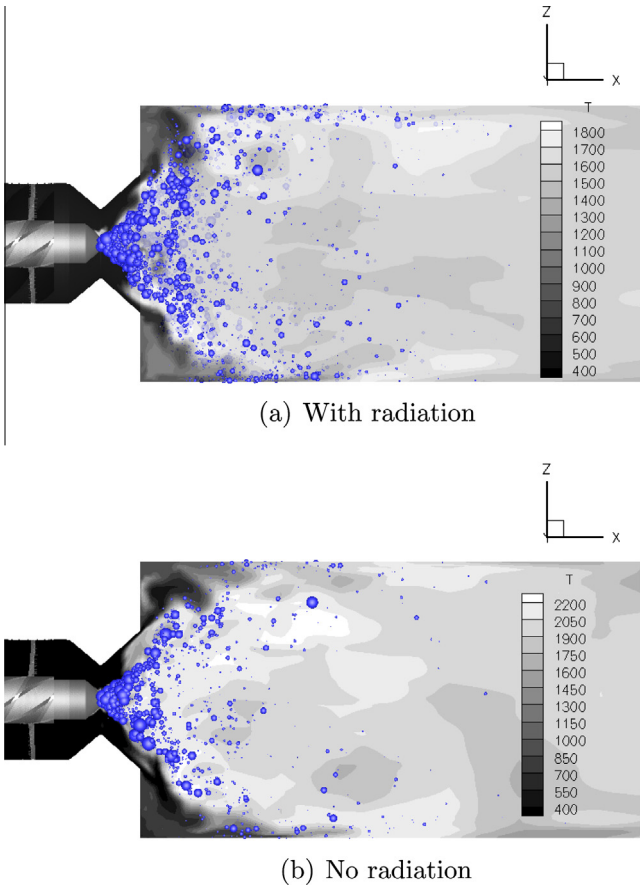

Fig. 6. Instantaneous droplet distribution sized by droplet mass combined with the instantaneous temperature distribution at the $y = 0$ plane.

To investigate the droplet size distribution, a comparison of the steady state droplet size histogram over the combustor volume is plotted in Fig. 8. In general, the case without radiation modeling has a lower number density especially for the larger size spectrum droplets. This explains the higher evaporation rate observed in Fig. 7b. The higher rate of evaporation leads to larger vapor fuel mass fraction (not shown here) and consequently will affect the local fuel mixture fraction, temperature distribution, and the species mass fraction.

4.3. Time averaged measurements and simulation data

Here the LES time averaged results with radiation modeling is compared with the experimental radial and axial profiles. The profiles with no radiation modeling will be shown when needed for comparison. Figure 9a and b shows spray droplet mean diameter D_{10} and Sauter mean diameter D_{32}. Overall good agreement is observed. At the first three axial locations a peak value is shown that starts at a radial distance of 8 mm from the centerline (for $x = 3$ mm) and then spreads radially towards the wall (for $x > 3$ mm). This location is an indication of the spray sheet cone angle. Since the spray droplets directly emitted from the injector have a large droplet size, the profiles show peak values at these radial locations. Downstream of $x = 15$ mm some droplets are trapped in the wall-corner vortex. It is interesting to note that the value of the mean diameter is increasing downstream due to evaporation of the smaller diameter droplets (larger than the cut-off value of the experimental measurements). This is consistent with the experimental data and other numerical observations [51].

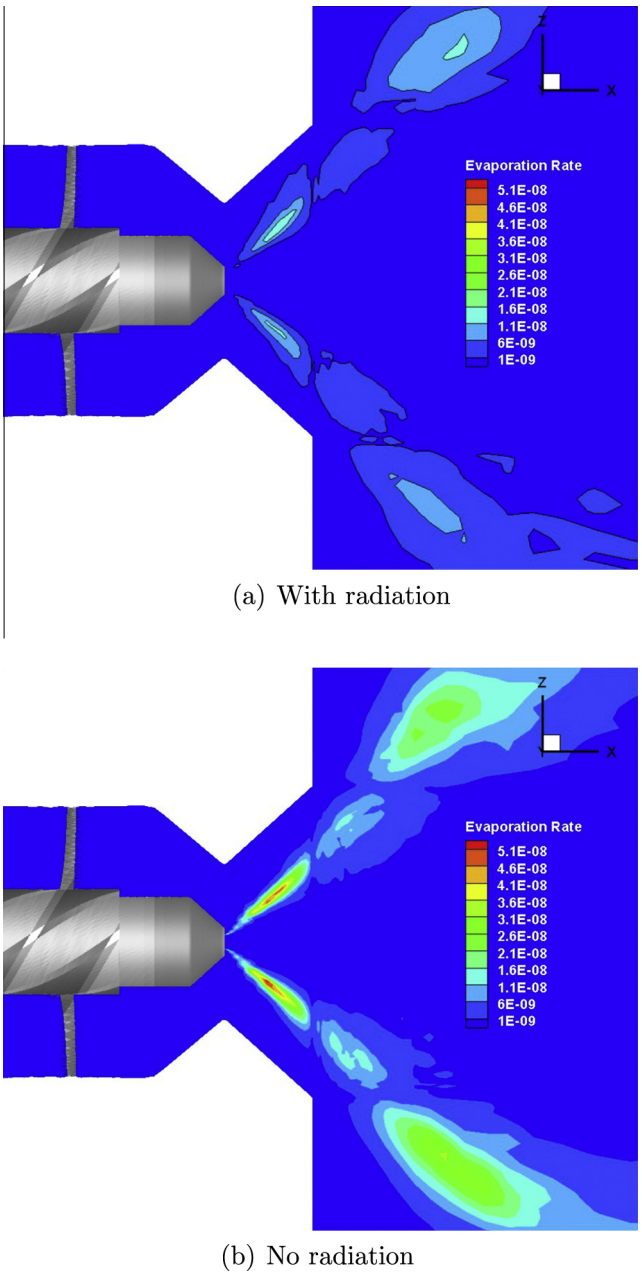

Fig. 7. Time-averaged droplet mass evaporation rate in (kg/s) at the central $y = 0$ plane. The figure shows that the droplets mass evaporation rate is over-predicted when radiation modeling is not included.

The spray droplets' mean axial velocity distribution is shown in Fig. 10. Good agreement is observed for all locations. Consistent with Fig. 9, the LES shows over-predicted droplet mean axial velocity at the locations of over-prediction in the droplet size. Again, over-prediction is expected at the first few locations, where the small-size droplets are not considered in the experiment.

To show the extent of the centerline RZ and the effect of heat release and radiation on the flow features, the centerline mean axial velocity profiles are shown in Fig. 11. Reactive and non-reactive data from experiments are compared with the LES results with and without radiation. The figure shows that the non-reactive RZ extends to about 100 mm downstream of the dump, while the reactive RZ is stronger and more compact (about 50 mm in length). The expansion of the flow by heat release changes the local velocity and pressure distribution. The local expansion (in the flame region)

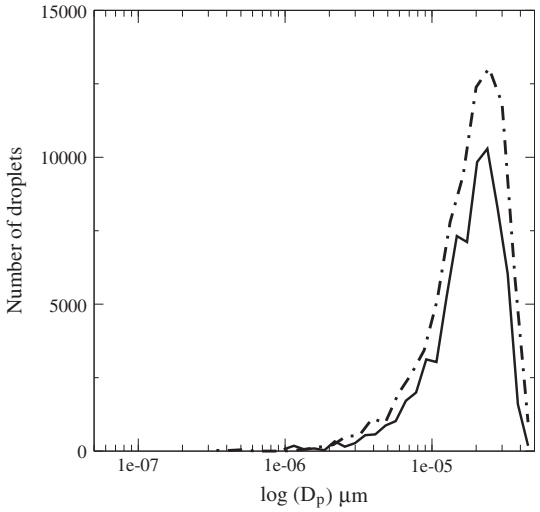

Fig. 8. Radiation effect on the droplet parcel histogram. (With radiation –·–·–, without radiation –).

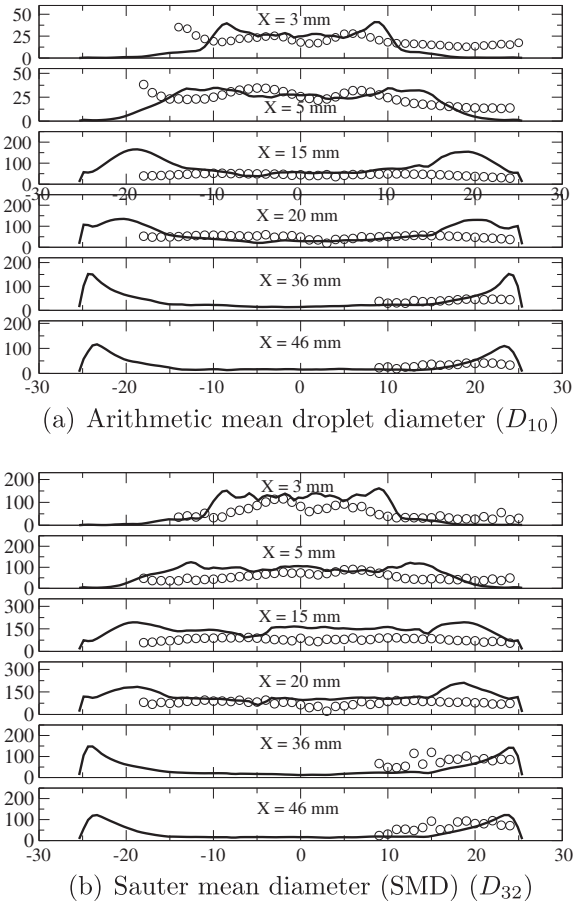

Fig. 9. Radial profiles of droplet arithmetic mean and Sauter mean diameters in μm (Experiment ∘, computation –)

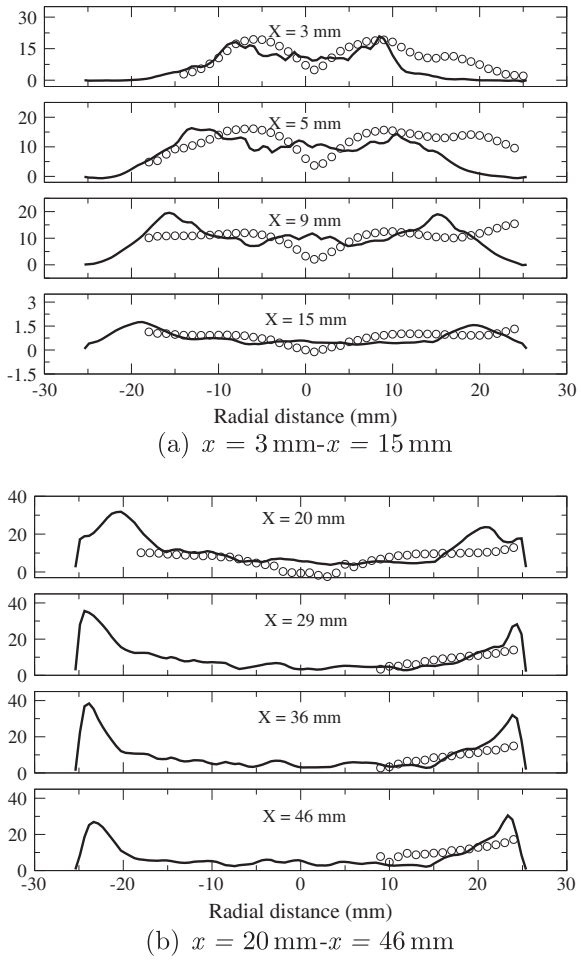

Fig. 10. Radial profiles of mean droplet axial velocity in *m/s* (Experiment ∘, computation –)

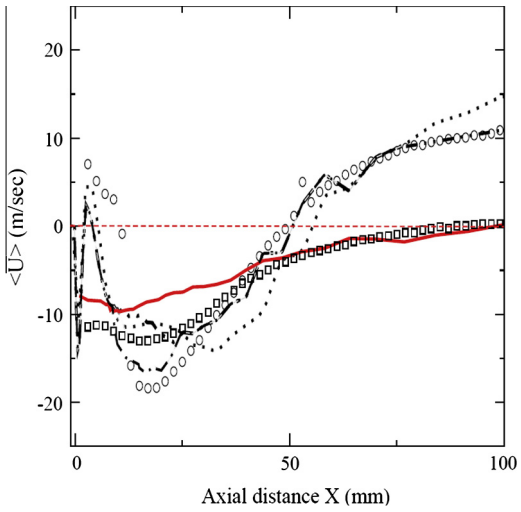

Fig. 11. Comparison of time-averaged centerline axial velocity $\langle\overline{U}\rangle$. Non-reactive flow (Experiment □, computation – –), reactive flow (Experiment ∘, computation with radiation –·–, computation with no radiation ...).

increases the pressure gradient and leads to faster flow deceleration. This results in a shorter but wider RZ. The CRZ without radiation is over-predicted by about 5 mm due to the change in the flame structure and the spray distribution.

As discussed below, the LES simulation shows that inside the divergent section of the Venturi a small RZ is established, followed by an increase in the velocity due to a sudden expansion downstream of the venturi. This is followed by a steep reduction inside the RZ due to the adverse pressure gradient. There are no experimental data inside the Venturi, but the profile captures the initial

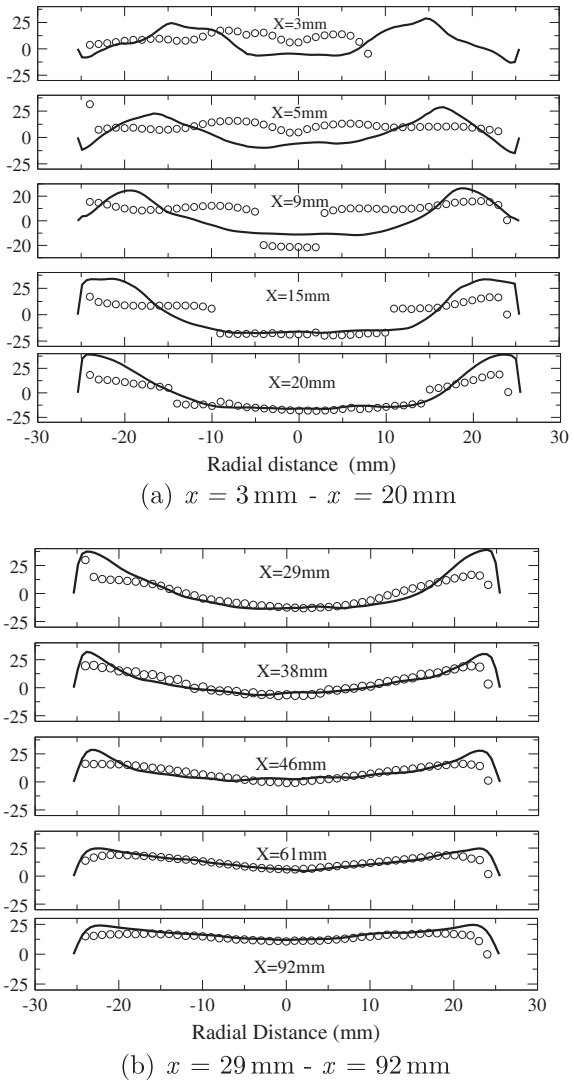

Fig. 12. Mean axial velocity $\langle \overline{U} \rangle$ at different axial locations in m/s (Experiment data ○, computation –).

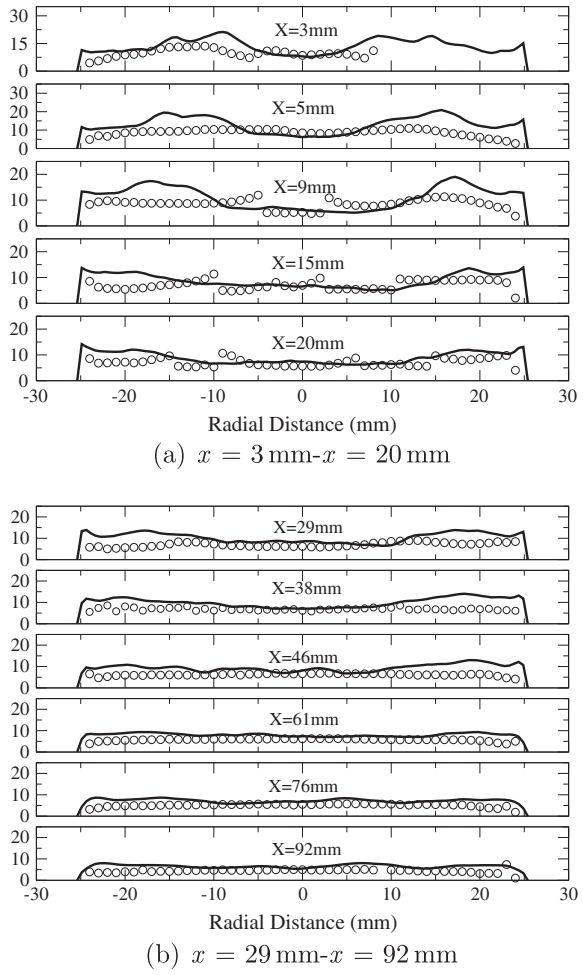

Fig. 13. RMS axial velocity U_{rms} at different axial locations in *m/s* (Experiment data ○, computation –).

peak after the dump accurately, which confirms the foregoing physical conclusions. Note that the current simulation captures the centerline profile initial peak. The deviations near the injector will be discussed later.

The mean and rms axial velocities are shown in Figs. 12 and 13. The first three locations ($x = 3$ mm, $x = 5$ mm and $x = 9$ mm) are found to be the most difficult to match with the experiment. These locations exhibit high unsteadiness and high measurement errors. The experimental measurements [29] use a Phase Doppler Particle Analyzer (PDPA). A problem usually related to the measurements is how to distinguish between the seed particles to measure the gas phase velocity and the spray droplets. In the LDI experimental measurements [29] the nominal diameter of the seed particles used was 1 μm. To distinguish between the spray and the seed particles, all particles smaller than 4 μm were used to represent the gas-phase velocity. However, inside the CRZ the small spray droplets just ejected from the nozzle still have high momentum in the positive direction. As a result, the experimental velocity profiles near the exit (i.e., $x = 3$ mm, $x = 5$ mm and $x = 9$ mm) are all positive despite the existence of the CRZ. Therefore, at these locations we expect to under-predict the experimental data. A previous RANS simulation [62] shows also higher deviation at $x = 3$ mm, and comparable results at $x = 9$ mm. The LES simulation by [25] also shows lower velocity at the location $x = 5$ mm. Starting from the $x = 15$ mm location, the current LES simulation shows good results compared with the experimental data. The CRZ extends to approximately 50 mm downstream of the dump. At the $x = 92$ mm location, the profile shows a nearly uniform velocity that recovers the inflow mass flow rate at the exit cross-sectional area. This uniformity is important in gas turbine engines to minimize the thermal stresses on the turbine blades. A slight deviation is found towards the walls. This can be attributed to the fact that the CRZ in the current simulation is wider than in the experiment. As a result, the flow is more compressed between the CRZ and the walls and the velocity is higher.

The rms axial velocity profile is shown in Fig. 14. The rms peaks close to the dump plane at the onset of the shear layer and then decays axially as the shear layer decays downstream. The predicted and experimental axial rms profiles show good agreement. The high rms values at the first three locations confirm the high unsteadiness of the shear layer. For example, at $x = 5$ mm the rms value is around 100% of the corresponding mean value. At the first three locations, over-prediction is noticed at the $y = 15$ mm radial location. The discrepancy with the experimental data at the first three locations is due to the reasons mentioned in the previous paragraph. The LES data predict two rms peaks that start at the radial location $y = 9$ mm at the first axial location. These two peaks spread downstream with the spread of the shear layer. Downstream of $x = 20$ mm, the peaks start to move again toward the centerline following the CRZ surface. After reaching the $x = 46$ mm

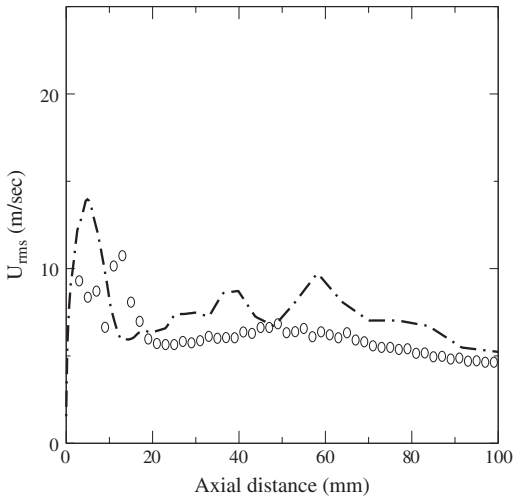

Fig. 14. RMS axial velocity along the centerline in m/s (Experiment data ∘, computation –).

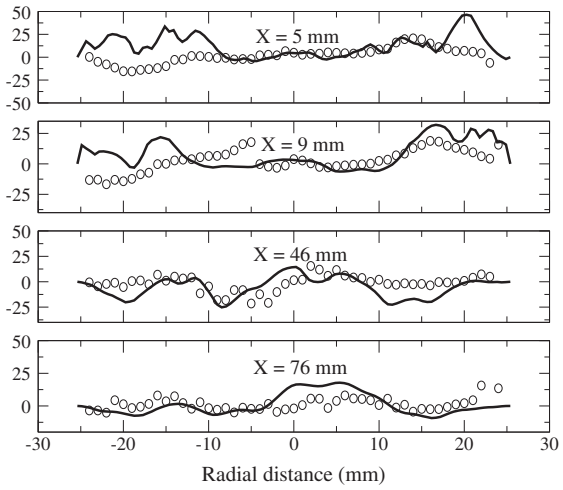

Fig. 15. Radial profiles of the shear stress $\widetilde{u''v''}$ in m^2/s^2.

location, the peaks are completely merged. After this location, no reverse flow exists and the shear layer is completely diffused. Similar observations apply to Fig. 15, where the radial profiles of the turbulent shear stress are plotted. The shear stress shows antisymmetric radial profiles. Good agrement is shown, with deviations at the first two locations. The zero shear stress at the centerline indicates flow symmetry around the centerline.

Figure 16 shows the mean velocity component in the y-direction at different axial locations. The flow is rotating in the counter-clockwise direction (CCW) viewed from the outflow cross-section. The global swirl number is of the order of 1. In contrast to other velocity components, the results show good agreement with the first location at $x = 3$ mm. The flow shows solid body rotation around the centerline downstream of the location $x = 29$ mm. Upstream of this location the flow is rotating around the central RZ.

For accurate prediction of the LDI emission characteristics, the temperature field has to be carefully predicted. For instance, NO production is a slow process and it is coupled with other processes that have long characteristic time scales such as radiation. Radiation, therefore, affects NO in an indirect way through the change in temperature, which then changes its production rates. Figure 17 shows the centerline mean temperature with and without radiation modeling. This figure shows that without radiation the temperature is over-predicted by about 200 K. This is consistent with earlier observations by Watanabe et al. [20] with DO radiation model. The radiation model employed here is an optically thin

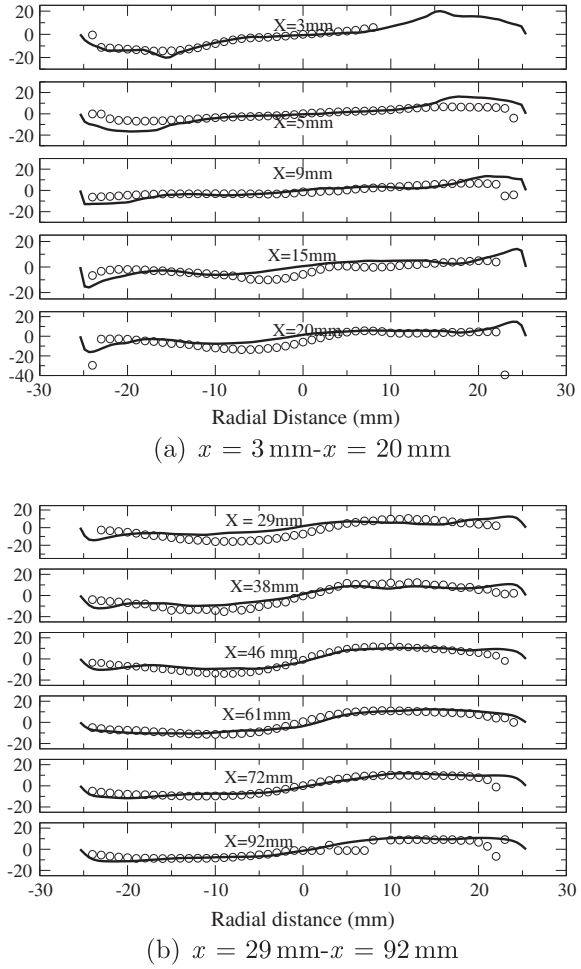

Fig. 16. Mean velocity component in the y direction $\langle \overline{U}_Y \rangle$ in m/s (Experiment data ∘, computation –).

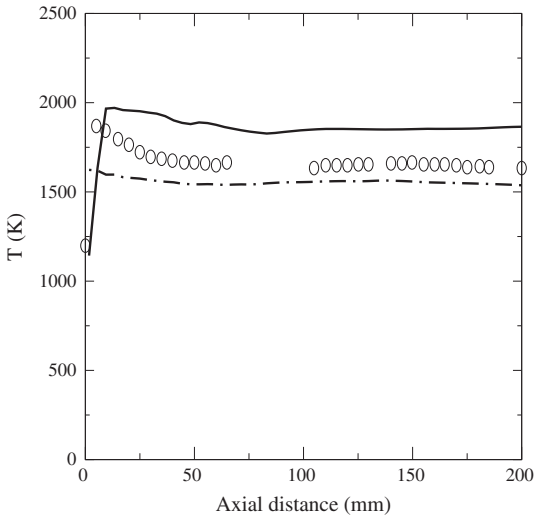

Fig. 17. Comparison of the centerline mean temperature $\langle \overline{T} \rangle$. (Experiment ∘, computation without radiation (–) and with radiation (· – ·).

model [46]. The model assumes that the medium is non-absorbing and neglects the heat lost or gained by wall absorption and reflection. The time averaged temperature spectrum on the Z–X plane is also shown in Fig. 18 for completeness. Figure 19 shows the radial temperature profiles comparison at the locations where experimental data are available with radiation modeling. Even with radiation modeling, the temperature is under-predicted at the centerline and shows larger deviation from experiment as we go closer to the wall and the shear layer. Temperature is also over predicted closer to the injector at $X = 5$ mm. This may suggest a need for a more accurate radiation model that accounts for the absorption within the flame, the scattering by the media (although might be negligible in this case), and the wall effect. Figure 20 shows the centerline species distribution for CO and NO mass fractions. With radiation modeling, slight under prediction is observed on a log-scale for NO and over prediction for CO mass fraction. As radiation modeling lowers the gas phase temperature and the evaporation rate to reduce the local mixture fraction distribution as discussed earlier, the species distribution retrieved from the table will also change. For example, radiation modeling effects, as shown in Fig. 20, are to increase the CO mass fraction and to lower the thermal NO production. The CO level along the centerline is captured reasonably well without radiation modeling and is over-predicted with radiation modeling. This is attributed to the simplifications in the combustion model, where the unsteady effects are neglected and fast chemistry is assumed. However, the centerline NO profile

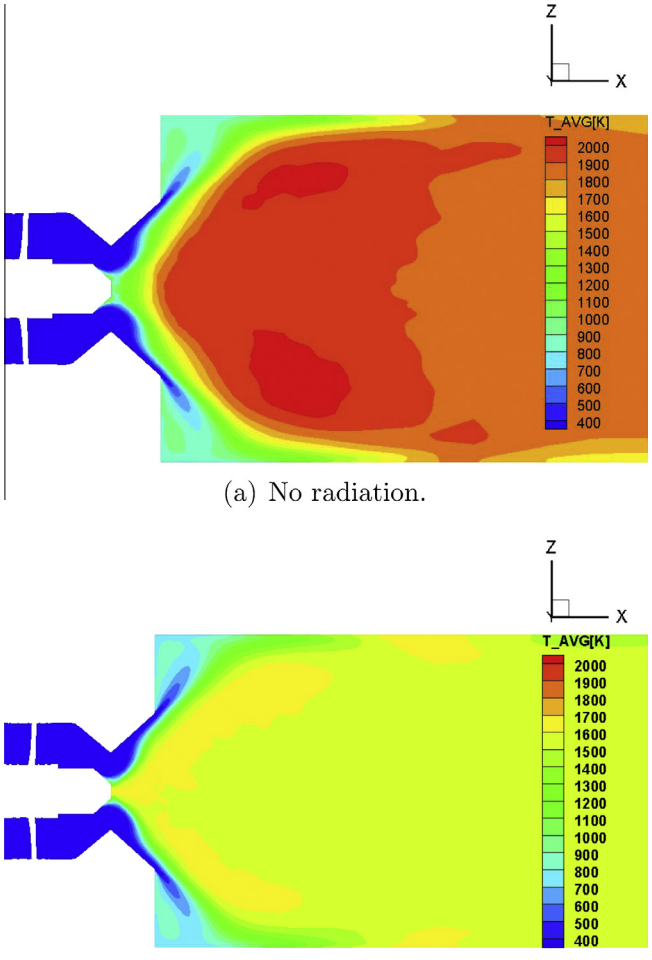

(a) No radiation.

(b) With radiation.

Fig. 18. Time averaged temperature spectrum $\langle \overline{T} \rangle$ in $K(y = 0$ plane).

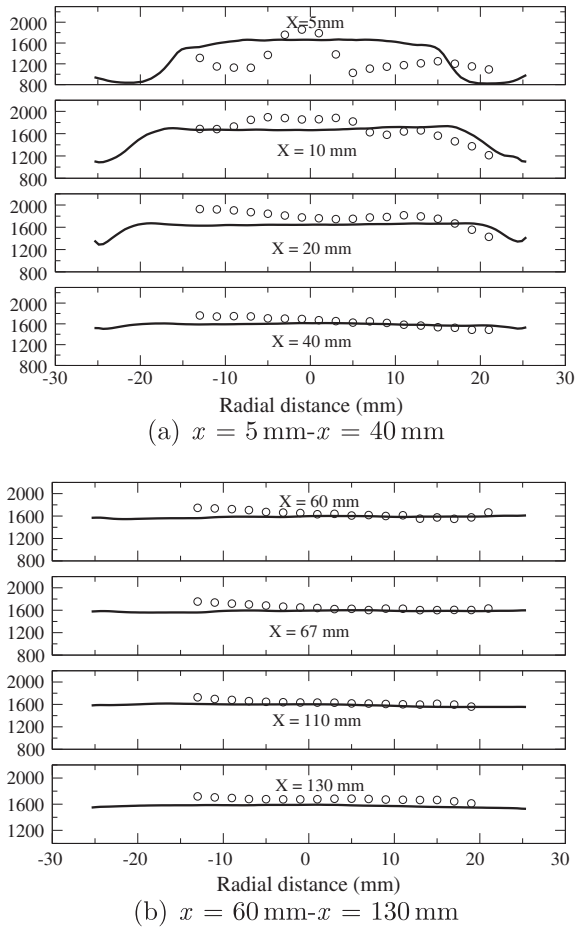

(a) $x = 5$ mm-$x = 40$ mm

(b) $x = 60$ mm-$x = 130$ mm

Fig. 19. Mean radial temperature profiles $\langle \overline{T} \rangle$ in K (Experiment ∘, computation –).

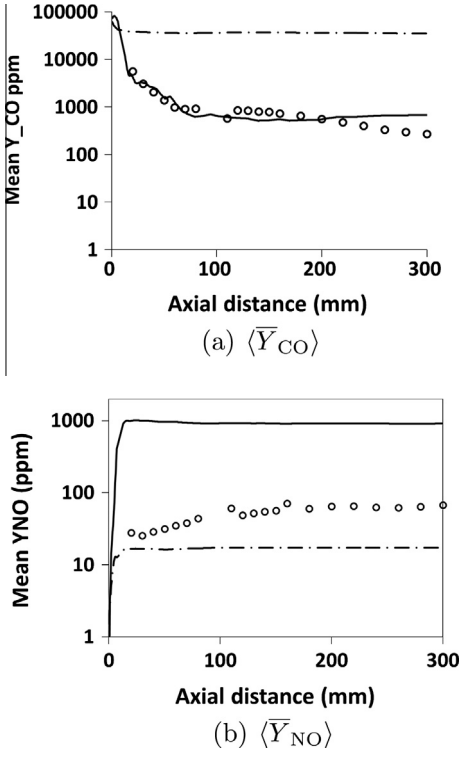

(a) $\langle \overline{Y}_{CO} \rangle$

(b) $\langle \overline{Y}_{NO} \rangle$

Fig. 20. Time averaged centerline species mass fractions profiles in ppm. The symbols are: Experimental measurements ∘, computation without radiation modeling (–) and with radiation modeling (·–·–·).

shows better prediction with radiation and over prediction with no radiation modeling. The better prediction for NO is a result of the more accurate temperature distribution and the unsteady interactions with the flow field predicted by Eq. (13). The FPV model radiation and NO modeling generally improves the NO predictions. In conclusion, the results show that radiation is important, with a maximum cooling effect of 400 K, with the truth somewhere in between the two simulations. Therefore, the good match of experimental data in T, CO, and NO can be due to compensating LES modeling errors, and/or due to the simplified radiation modeling effect. With 400 K loss due to radiation emissions, the flame might not be optically thin in nature. Large amounts of emission from combustion gases with strong spectral bands can be accompanied by substantial absorption, in particular with the presence of droplets that are preheated by radiation. The study, however, suggests the need for more rigorous treatment for radiation and the unsteady interactions between chemistry and the flow field.

5. Conclusions

Large eddy simulations for a Jet-A liquid fuel LDI combustor are performed and compared with the experimental measurements. The current paper represents one of the most complete comparisons for this LDI configuration with both radiation and spray coupling. Good comparisons for the gas-phase and spray measurements are shown, except for the first few locations close to the injector, where the small-size droplets are not considered in the experiment and where the flow exhibits high unsteadiness. The high rms values at the first three locations confirm the high unsteadiness of the shear layer, where the rms value is around 100% of the corresponding mean value. The non-reactive RZ was found to extend to about 100 mm downstream of the dump, while the reactive RZ is stronger and more compact (about 50 mm in length). The CRZ without radiation is found to be over-predicted by about 5 mm due to the change in the flame structure and the spray distribution. Downstream of $x = 15$ mm some droplets are found to be trapped in the wall-corner vortices. The results show that the flow shows solid-body rotation in the clockwise direction downstream of the location $x = 29$ mm (viewed from the outflow cross-section) with a global unity swirl number. Upstream of this location the flow is rotating around the central RZ that acts as a stabilizing bluff-body for the flame.

The simulations show that LDI design is a good candidate for low emissions, yet stable, gas turbine engines. Radiation modeling is found to be essential for more accurate temperature, and spray dynamics predictions. By changing the heat release distribution and local temperature, radiation alters the spray evaporation rate and the droplets size distribution. The variation in the local mixing ratio changes the scalar field and the combustion heat release rate. Thus, radiation modeling can be important even for low pressure systems where radiation from flame region is expected to be relatively small. The local effect on the spray size distribution is found to affect the simulations predictions through the air/fuel ratio in the gas phase. The temperature, however, is found to be under-predicted at the centerline and as we approach the wall and the injector head which suggests the need for a more accurate radiation model that accounts for the absorption within the flame, the scattering by the media (although might be negligible in this case), and the non-adiabatic wall effects. The radiation modeling effects on species predictions are found to over-predict CO and slightly under-predict NO mass fractions. However, NO mass fraction was significantly improved with radiation modeling. This also reveals the effect of the simplifications in the combustion model on the pollutants predictions, where the unsteady flame interactions with the flow field are not accounted for. Future simulations will focus on more accurate radiation modeling and how unsteady combustion modeling can improve the pollutants predictions. In general, the simulations show the promising ability of LES as a numerical tool to simulate multi-physics problems in complex flows.

Acknowledgments

This work is funded by NASA Glenn Research Center. The authors thanks Nan-Suey Liu for providing advice, grid and experimental data for comparison. Many thanks to Heinz Pitsch for his continuous support and revision for this manuscript and for his helpful discussions and technical advice. The authors also acknowledge Frank Ham from Stanford for his valuable support with the CDP code and Jeffrey P. Moder from GRC for reviewing the final version of the manuscript.

Appendix A. Supplementary data

Supplementary data associated with this article can be found, in the online version, at http://dx.doi.org/10.1016/j.combustflame.2013.09.020.

References

[1] A.H. Lefebvre, Gas Turbine Combustion, second ed., Taylor & Francis, London, UK, 1999.
[2] G.M. Faeth, G. Roth, M. Gundersen, in: G. Roy (Ed.), Propulsion Combustion: Fuels and Emissions, Taylor & Francis, Washington, DC, 1998, pp. 359–407.
[3] C.K. Law, Combustion Physics, Cambridge University Press, New York, USA, 2006.
[4] S.V. Apte, V. Yang, Combust. Flame 131 (2002) 110–131.
[5] S. Menon, in: T. Lieuwen, V. Yang (Eds.), Combustion Instabilities in Gas Turbine Engines: Operational Experience, Fundamental Mechanisms, and Modeling, AIAA Progress in Aeronautics and Astronautics, vol. 210, 2005, pp. 277–314.
[6] H. El-Asrag, H. Pitsch, W. Kim, H. Do, M.G. Mungal, Combust. Sci. Technol. 183 (2011) 718–737.
[7] Pratt & Whitney, General-Electric, NASA Critical Report: NASA/CR-2005-213584/vol. 1, 2005.
[8] K.-S. Im, M.C. Lai, R.R. Tacina, 34th AIAA/ASME/SAE/ASEE Joint Propulsion Conference and Exhibit, Cleveland, Ohio AIAA 1998-3269, 1998.
[9] H. El-Asrag, A.C. Iannetti, NASA Technical Report: NASA/TM-2011-217111, E-17787, 2011.
[10] T.J. Poinsot, D. Veynante, Theoretical and Numerical Combustion, second ed., R.T. Edwards, Inc., Philadelphia, PA, USA, 2005.
[11] C.K. Law, Proc. Combust. Inst. 31 (2007) 1–29.
[12] N. Peters, Proc. Combust. Inst. 32 (2008) 1–25.
[13] G. Boudier, L. Gicquel, T.J. Poinsot, Combust. Flame 155 (2008) 196–214.
[14] P. Pepiot-Desjardins, H. Pitsch, Combust. Flame 154 (2008) 740–760.
[15] H. El-Asrag, Y. Ju, Combust. Theory Model. 17 (2013) 316–334.
[16] H. El-Asrag, Y. Ju, Combust. Flame (2013), http://dx.doi.org/10.1016/j.combustflame.2013.07.012.
[17] M.A. Mueller, R.A. Yetter, F.L. Dryer, Int. J. Chem. Kinet. 32 (2000) 317–339.
[18] M. Herrmann, Phys. Fluids 23 (2011) 0911089.
[19] S.V. Apte, K. Mahesh, M. Gorokhovski, P. Moin, Proc. Combust. Inst. 32 (2008) 2257–2266.
[20] H. Watanabe, R. Kurose, S. Komori, H. Pitsch, Combust. Flame 152 (2008) 2–13.
[21] N. Peters, Turbulent Combustion, Cambridge University Press, Cambridge, UK, 2000.
[22] H. Pitsch, Annu. Rev. Fluid Mech. 38 (2006) 233–266.
[23] H. El-Asrag, S. Menon, Proc. Combust. Inst. 31 (2007) 1747–1754.
[24] H. Pitsch, O. Desjardins, G. Balarac, M. Ihme, 46th AIAA Aerospace Sciences Meeting and Exhibit, Reno, Nevada, January 7–10, 2008 AIAA-2008-604, 2008.
[25] N. Patel, S. Menon, Combust. Flame 153 (2008) 228–257.
[26] J. Galpin, A. Naudin, L. Vervisch, C. Angelberger, O. Colin, P. Domingo, Combust. Flame 155 (2008) 247–266.
[27] R.R. Tacina, C. Wey, K.J. Choi, 37th AIAA/ASME/SAE/ASEE Joint Propulsion Conference and Exhibit, Salt Lake City, Utah AIAA 2001-34065, 2001.
[28] S.L. Yang, Y.K. Siow, B.D. Peschke, R.R. Tacina, J. Eng. Gas Turbine Power 125 (2003) 804–811.
[29] J. Cai, S.-M. Jeng, R.R. Tacina, 43rd AIAA Aerospace Science Meeting and Exhibit, AIAA, Reno, Nevada, 2005, pp. 2005–1425.
[30] R. Mehta, D.C. Haworth, M.F. Modest, Combust. Flame 157 (2010) 982–994.
[31] A. Habibi, B. Merci, D. Roekaerts, Combust. Flame 151 (2007) 303–320.
[32] M. Modest, Int. J. Multiscale Comput. Eng. 3 (2005) 85–105.
[33] P. Coelho, T.O.J., D. Roekaerts, Combust. Flame 156 (2009) 1099–1110.
[34] P. Coelho, Combust. Flame 156 (2009) 1099–1110.
[35] P. Coelho, Prog. Energy Combust. Sci. 33 (2007) 311–383.

[36] R. Santos, M. Lecanu, S. Ducruix, O. Gicquel, E. Iacona, D. Veynante, Combust. Flame 152 (2008) 387–400.
[37] P. Desjardins, S. Frankel, Combust. Flame 119 (1999) 121–132.
[38] W.P. Jones, M.C. Paul, Int. J. Eng. Sci. 43 (2005) 379–397.
[39] H. Watanabe, R. Kurose, S.-M. Hwang, F. Akamatsu, Combust. Flame 148 (2007) 234–248.
[40] F. Ham, in: Annual Research Briefs., Stanford Calif.: Center for Turbulence Research, 2007, pp. 41–45.
[41] H. El-Asrag, F. Ham, H. Pitsch, in: Annual Research Briefs., Stanford Calif.: Center for Turbulence Research, 2007, pp. 241–253.
[42] C.D. Pierce, P. Moin, J. Fluid Mech. 504 (2004) 73–97.
[43] S. Ghosal, T. Lund, P. Moin, K. Akselvoll, J. Fluid Mech. 286 (1995) 225–229.
[44] S. Honnet, K. Seshadri, U. Niemann, N. Peters, Proc. Combust. Inst. 32 (2008) 485–492.
[45] M. Ihme, H. Pitsch, Combust. Flame 155 (2008) 90–107.
[46] M. Ihme, H. Pitsch, Phys. Fluid 20 (2008) 0055110–0055120.
[47] S.V. Apte, M. Gorokhovski, P. Moin, Int. J. Multiphase Flow 29 (2003) 1503–1522.
[48] M. Ihme, C.M. Cha, H. Pitsch, Proc. Combust. Inst. 30 (2008) 793–800.
[49] M. Ihme, H. Pitsch, Combust. Flame 155 (2008) 70–89.
[50] R.W. Bilger, Combust. Flame 80 (1990) 135–149.
[51] M. Nakamura, F. Akamatsu, R. Kurose, M. Katsuki, Phys. Fluids 17 (2005) 123301.
[52] P.D. Ronney, in: H. Ross (Ed.), Microgravity Combustion: Fires in Free Fall, Academic Press, London, UK, 2001, pp. 35–82.
[53] G.L. Hubbard, C.L. Tien, Heat Transfer 100 (1978) 235–239.
[54] R. Barlow, A. Karpetis, J. Frank, J.-Y. Chen, Combust. Flame 127 (2001) 2102–2118.
[55] S.V. Apte, K. Mahesh, P. Moin, Proc. Combust. Inst. 32 (2008) 2247–2256.
[56] C.T. Crowe, J. Scwarzkopf, M. Sommerfeld, Y. Tsuji, Multiphase flows with droplets and particles, CRC Press, 1998.
[57] G. Faeth, Prog. Energy Combust. Sci. 7 (1983) 1–76.
[58] C. Law, Prog. Energy Combust. Sci. 8 (1982) 171–201.
[59] W. Sirignano, C. Law, in: Evaporation-Combustion of Fuels: A Symposium, American Chemical Society, 1978.
[60] R. Miller, K. Harstad, J. Bellan, Int. J. Multiphase Flow 24 (1998) 1025–1055.
[61] D. Farhad, N.-S. Liu, P.M. Jeffrey, NASA Technical Report: NASA/TM-2006-214252, 2006.
[62] A.C. Iannetti, N.-S. Liu, D. Farhad, NASA Technical Report: NASA/TM-2008-215422, 2008.
[63] M. Herrmann, J. Comput. Phys. 229 (2010) 745–759.